A novel feedback correction-adaptive Kalman filtering method for the whole-life-cycle state of charge and closed-circuit voltage prediction of lithium-ion batteries based on the second-order electrical equivalent circuit model.

WANG, S., TAKYI-ANINAKWA, P., FAN, Y., YU, C., JIN, S., FERNANDEZ, C. and STROE, D.-I.

2022

A novel feedback correction-adaptive Kalman filtering method for the whole-life-cycle state of charge and closed-circuit voltage prediction of lithium-ion batteries based on the second-order electrical equivalent circuit model

Shunli Wang[1], Paul Takyi-Aninakwa[1], Yongcun Fan[1], Chunmei Yu[1], Siyu Jin[2], Carlos Fernandez[3], Daniel-Ioan Stroe[2]

[1]School of Information Engineering & Robot Technology used for Special Environment Key Laboratory of Sichuan Province, Southwest University of Science and Technology, Mianyang, 621010, China.

[2] Department of Energy Technology, Aalborg University, Pontoppidanstraede 111, 9220 Aalborg East, Denmark.

[3]School of Pharmacy and Life Sciences, Robert Gordon University, Aberdeen AB10-7GJ, UK.

Abstract: Accurate state of charge (SOC) and closed-circuit voltage (CCV) prediction is essential for lithium-ion batteries and their model performance. In this study, a novel feedback correction-adaptive Kalman filtering (FC-AKF) method is proposed for the online battery state co-prediction, which is adaptive to the whole-life-cycle of the lithium-ion battery based on the improved second-order equivalent circuit model (SO-ECM). For the feedback correction strategy, the optimized iterative state initialization is conducted using the uncertainty covariance matrix of the prior three-time points with the convergence of the updating process. The experimental results show that the SOC prediction error of the proposed FC-AKF method is 0.0099% and 0.975% compared with the ampere-hour integral method under the dynamic stress test (DST) and the Beijing bus dynamic stress test (BBDST) working conditions, respectively. Also, the CCV traction by the SO-ECM is 0.80 V and has fast initial convergence and quick prediction error reduction characteristics. The constructed iterative calculation model promotes the accurate SOC and CCV co-prediction effect, improving the safety and longevity of lithium-ion batteries with high precision and fast convergence advantages.

Keywords: state of charge; closed-circuit voltage; second-order equivalent circuit model; feedback correction-adaptive Kalman filter; whole-life-cycle variation; fast initial convergence

Corresponding author: Shunli Wang, wangshunli@swust.edu.cn

Highlights

- A novel feedback correction-adaptive Kalman filtering (FC-AKF) method is proposed for the online SOC and CCV co-prediction, which is adaptive to the whole-life-cycle temperature and current rate variations of lithium-ion batteries.

- An improved second-order equivalent circuit model (SO-ECM) is constructed by introducing two resistor-capacitor circuits to characterize the electrochemical and concentration polarization effects.

- A state initialization, iterative time update, and error covariance matrix correction are investigated using the uncertainty matrix at a priori three-time point.

- The constructed SO-ECM and FC-AKF model promote the accurate state co-prediction effect with a maximum error of 0.0099% and 0.975% under the dynamic stress test (DST) and the Beijing bus dynamic stress test (BBDST) working conditions, respectively, improving the safety and longevity of lithium-ion batteries.

1. Introduction

Rapid industrial development has brought economic prosperity, along with environmental pollution and an energy crisis. Lithium-ion batteries have a high energy density, a long lifespan, and high terminal voltage advantages and have greatly supported the power storage and supply process. Consequently, lithium-ion batteries have become an indispensable energy storage system that applies to most of the technological fields. The state of charge (SOC) and closed-circuit voltage (CCV) prediction are critical thresholds for safe and high-efficiency charge-discharge maintenance [1], in which accurate state prediction helps to extend the service life of lithium-ion batteries.

Equivalent circuit models (ECMs) play a significant role in the state prediction process of lithium-ion batteries. The Rint model only includes the ideal voltage source and internal resistance, but the polarization characteristics are not considered effectively [2]. For the cyclic charge-discharge process, the polarization effect is generated and increases with the current rate to influence the SOC prediction accuracy, which is affected by the variation of temperature, self-discharge, aging, and other factors in highly nonlinear conditions. The modeling mechanism and internal short circuit prevention are considered, including stress-driven quantifying and equivalent circuit model (ECM) [3, 4]. Direct and indirect anode ECMs are constructed through internal short-circuiting and venting in the thermal runaway processes to directly predict the cathode potential based on cathode parameter identification and an indirect anode potential prediction under different working conditions [5]. Nonlinear characteristics are considered for the battery cells using the Hammerstein-Wiener model to accurately predict the behavior of these cells [6]. The supervised machine learning model is constructed based on the second-order ECM (SO-ECM) to achieve an accurate fault diagnosis for batteries of electric aircraft under different test conditions [7]. A confidence-interval-based prognostic model is proposed to quantify and assess the practical parameter identification ability of the SO-ECM using profile likelihood and ratio subset statistics [8]. A fractional-order ECM is established for multiple lithium-ion batteries under different states based on electrochemical impedance spectroscopy (EIS) analysis [9]. The reduced electrochemical model is introduced to realize the condition monitoring in the advanced battery management systems [10]. A novel mesoscale electrothermal is established to simulate the electrical characteristics of a whole battery by capturing the current and terminal voltage of each constituent cell sandwich [11]. The electro-thermal coupled model is established by considering the electric potential, heat generation, and distribution [12].

Key parameters of the ECM are determined by experimental data from the hybrid pulse power characteristic (HPPC) tests to

obtain the ohmic resistance value with the instantaneous dynamic terminal voltage variations from the start to the end of the charge-discharge process. The internal polarization resistance and capacitance are obtained through the slow terminal voltage variation analysis [13]. A thermoelectric coupling model is established for the SOC prediction based on the physical-based high-frequency modeling of the time-domain battery characteristics [14]. The challenges of the data-based degradation model are analyzed for the long-term aging characteristic description for lithium-ion batteries [15]. With the feedback structure of the Doyle-Fuller-Newman model, the analysis using the input-output systems theory was conducted [16]. An improved simulated annealing method to access the uncertain states and an adaptive switch mechanism to adjust the prediction of an adaptive extended Kalman filter (AEKF) algorithm for SOC prediction based on the SO-ECM with no correction factor [17]. A numerical mechanics model of lithium-ion batteries is established to imperatively study their mechanical integrity and internal short circuit by considering the SOC and dynamic behaviors under different loading conditions [18]. A lumped-parameter two-state electro-thermal model for lithium-ion batteries is established based on a temperature-dependent SO-ECM and a joint Kalman filter core temperature prediction [19]. An integrated electro-thermal model is proposed to predict the thermal characteristics of a battery cell-based only on its current and ambient conditions and validated through the tuning of experimental results [20]. The effect of measurement noise on model parameter identification and SOC prediction is investigated by a parameterization method combining instrumental variable prediction and the bilinear principle [20]. A singularly perturbed phase-field model is used to model lithium-ion batteries by considering factors such as chemical and elastic effects [21].

Commonly used prediction methods, such as the Ampere-hour (Ah) integral method, have a large error. The open-circuit voltage (OCV) method is mainly used for offline state prediction and is highly dependent on the initial SOC value. High-precision methods include data-driven methods such as feedforward neural network (NN), fuzzy logic, long short-term memory (LSTM), etc., and model-based methods, including Kalman filtering (KF) algorithms, etc., for SOC prediction. The KF as a model-based method is an optimum regression data processing method that realizes the optimal state variable prediction in real-time. The extended Kalman filtering (EKF) algorithm introduces a first-order Taylor series expansion of the nonlinear system to linearize it and improve the prediction accuracy by ignoring the high-order terms. Thus, the nonlinear system is linearized to adapt to the nonlinear battery system [22]. An improved log-linear method is constructed for extracting, modeling, and predicting the resistance of lithium-ion batteries from dynamic aging profiles based on the measured internal resistance and the SOC value [23]. A three-dimensional electrochemical-thermal coupling model of a lithium-ion battery is constructed to study the electrochemical distribution characteristics of the electrode and its evolution factors [24]. The SOC and the state of power (SOP) are jointly predicted under multiple constraints using the dual-polarization (DP) model with the EKF to improve the accuracy of the prediction [25]. A model-based observer is used to analyze the possible error sources in the SOC prediction of lithium-ion batteries in real-time applications [26]. The ECM of a lithium-ion battery is established to analyze the EIS response to the SOC prediction based on the determining

factors of the ECM parameters [27]. Online parameter identification is constructed to analyze the different influences of voltage and current noise on the SOC prediction [28]. A multi-scale prediction method is established for the remaining useful life (RUL) and SOH by a combined wavelet neural network-unscented particle filter (WNN-UPF), on which the SOC of the lithium-ion battery is dependent [29]. A gated recurrent unit recurrent neural network with activation function layers (GRU-ATL) is established to predict the SOC using deep learning technology to establish the nonlinear relationship between the measured current, voltage, and temperature signals and the battery SOC [30].

In the battery management system (BMS), sampling signals are affected by the uncertainty noise reduction introduced by the variants of the KF for SOC prediction. The SO-ECM is proposed based on an improved EKF and an adaptive unscented Kalman filter (AUKF) to accurately predict the SOC with a maximum error of 2.30% and 3.30%, respectively, due to their noise reduction effect [31, 32]. The KF-based methods track the nonlinear SOC value precisely. By factoring in robustness, adaptability, and reduced noise by the error covariance matrix, low computational complexity is achieved with high accuracy in the SOC prediction. The unscented transform is introduced, in which a certain number of sampling data points are selected according to the statistical characteristics of state variables. Through the establishment of the ECM, the functional OCV-SOC relationship is obtained to construct the systematic mixed adaptive observer for the prediction model at varying conditions [33, 34]. Adaptive prediction is realized via simplified single-particle modeling [35] so that the initialization converges. Consequently, the prediction error decreases and is stable in the whole-life-cycle procedure. An enhanced battery model is constructed to predict the degraded capacity by the optimized EKF calculation [36]. Asymptotic reduction and homogenization are analyzed for the thermo-electrochemical [37] and pure electrochemical [38] models.

For electric vehicle applications, the adaptive Lyapunov super twisting observer and adaptive extended Kalman filters (AEKFs) are established to ensure an accurate prediction of the SOC with an enhanced parameter identification method such as a dual forgetting factor [39-41]. The accurate SOC estimation is realized by using the fractional-order calculus strategy [42]. A strict Lyapunov super twisting observer is designed [43], and adaptive prediction methods are modeled by FBG-based strain sensing and machine learning [44] for robust SOC prediction. Also, a polynomial augmented-extended Kalman filter (PA-EKF) is conducted for [45], and an integral-type terminal sliding-mode observer [46] is constructed for the robust prediction. An improved least square-support vector regression (LS-SVR) [47] is established with an online sequential extreme machine learning [48] and anomaly detection, Levenberg-Marquardt, and multiphase exponential regression model [49]. The SOC prediction is realized with limited data [50], the GRU neural network [51], differential temperature conditions [52], the LSTM neural network [53], and the incremental capacity technique [54]. The sequential model is realized by active current injection [55]. A health-aware multi-objective optimal charging model is established to simultaneously shorten the charging time and relieve the battery degradation based on a coupled electrochemical-thermal-aging battery model [56]. The prediction is realized by data fusion treatment and

multi-objective optimization of the data-driven model, which is modeled with short-term features. The battery life prediction is realized by hybrid modeling, and the prediction framework is constructed by combining PF with the sliding window gray model. Deep reinforcement learning-based energy storage [57] is also realized by accurate degradation modeling. A tailoring life cycle study of lithium-ion batteries is conducted under a passive cooling system [58]. Quantitative analysis of performance decreases and fast-charging limitations is realized for low-temperature conditions by electrochemical modeling [59]. Advanced modeling is realized for hybrid energy storage systems integrating lithium-ion batteries and supercapacitors [60]. Mathematical modeling is realized to obtain frequency-domain characteristics of periodic pulse-discharged battery systems [61]. Consequently, the external battery characteristics are described accurately by nonlinear models with online parameter identification.

Due to the urgent application requirement, the improved SO-ECM combined with the feedback correction-adaptive Kalman filter (FC-AKF) is proposed for online co-prediction of SOC and CCV that is adaptive to the whole-life-cycle battery characteristic variation. A high-precision observer is established for the state prediction by the ECM and iterative correction of the FC-AKF. The proposed nonlinear SO-ECM describes the external battery characteristics accurately, in which two resistor-capacitor (RC) circuits are introduced to describe the electrochemical and concentration polarization effects. For the proposed FC-AKF method, state initialization, iterative time update, and covariance correction are investigated using the uncertainty matrix during the prior time update. The Kalman gain calculation and state observation are realized to correct the state prediction values at each time point so that the prediction accuracy is improved by recursively updating the measured and predicted variables, making the predicted value converge.

2.   Mathematical Analysis

By considering the aging characteristics under wide temperature range conditions, the collaborative battery SOC and CCV prediction are realized by SO-ECM and iterative calculation of the FC-AKF for the whole-life-cycle of lithium-ion batteries with adaptive parameter correction.

2.1.   Second-order equivalent circuit modeling

Compared with the partnership for new generation vehicles (PNGV), general nonlinear (GNL), and other battery models, the proposed SO-ECM has a simple structure and belongs to the nonlinear reduced-order types with few parameters and high accuracy that is adaptive to the dynamic characteristics of the lithium-ion batteries. The polarization influence on voltage is considered by introducing one more RC circuit so that the dynamic behavior is effectively characterized. Then, the nonlinear state-space equation is established to construct the whole structure of the SO-ECM to predict the battery state with high accuracy. The framework of the SO_ECM is constructed as shown in Figure 1.
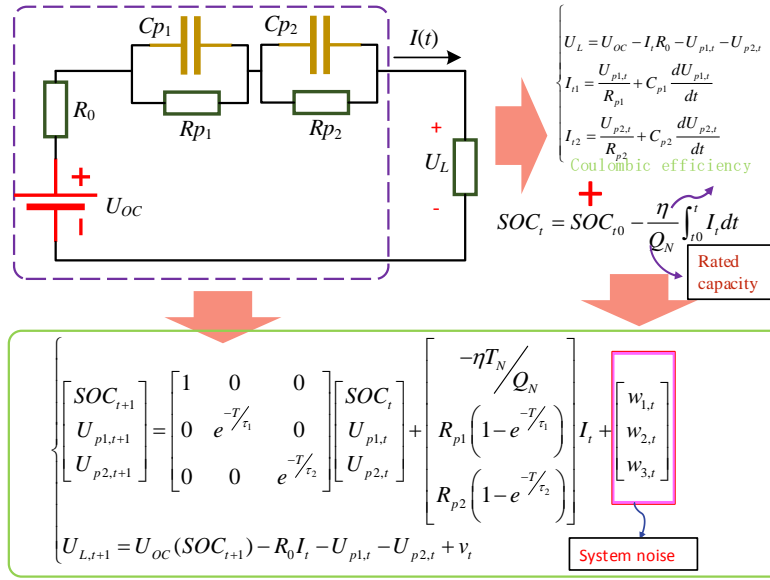
Figure 1. The framework of the second-order equivalent circuit model

In Figure 1, the U_{OC} source is the battery's open-circuit voltage (OCV) characteristics, and U_L is the battery terminal voltage. R_0 is the ohmic resistance. R_{p1} and R_{p2} are the battery's electrochemical and concentration polarization resistance effects, respectively. C_{p1} and C_{p2} are the battery's electrochemical and concentration polarization capacitance effects, respectively. $I(t)$ is the charge-discharge current.

2.2. State-space equation of the improved SO-ECM

By the improved SO-ECM, U_L and I_t are obtained the mathematical relationship of the electrical components according to Kirchoff's circuit law, as shown in Equation (1).

$$\begin{cases} dU_{p1}/dt = I_t/C_{p1} - U_{p1}/R_{p1}C_{p1} \\ dU_{p2}/dt = I_t/C_{p2} - U_{p2}/R_{p2}C_{p2} \\ U_L = U_{OC}(SOC_t) - I_t R_0 - U_{p1} - U_{p2} \\ \tau_1 = R_{p1}C_{p1}; \tau_2 = R_{p2}C_{p2} \end{cases} \tag{1}$$

In Equation (1), U_{OC} is theoretically equal to the OCV value, and its mathematical expression is $U_{OC} = f(SOC_t)$ for the SOC variation. The frequency-domain expression of the SO-ECM is obtained by the Laplace transform, as shown in Equation (2).

$$E(s) = U_{OC}(s) - U_L(s) = I(s)\left[R_0 + \frac{R_{p1}}{1 + R_{p1}C_{p1}s} + \frac{R_{p2}}{1 + R_{p2}C_{p2}s}\right] \tag{2}$$

In Equation (2), $E(s)$ is the voltage variation between the OCV factor $U_{OC}(s)$ and the CCV factor $U_L(s)$, which is mainly caused by three effects, including R_0, $R_{p1}C_{p1}$, and $R_{p2}C_{p2}$. The discretization of the mathematical relationship for these parameters is conducted using the bilinear transformation, as shown in Equation (3).

$$E(t) = \theta_1 E(t-1) + \theta_2 E(t-2) + \theta_3 I(t) + \theta_4 I(t-1) + \theta_5 I(t-2) \tag{3}$$

In Equation (3), the electro power of $E(t)$ is obtained using the parameters $E(t-1)$, $E(t-2)$, $I(t)$, $I(t-1)$, and $I(t-2)$

with the coefficients varying from θ_1 to θ_5.

Taking S_t as the SOC value at the time point t, the SOC value is obtained by the Ah integral method in the prediction step, as

shown in Equation (4).

$$S_t = S_{t_0} - \frac{1}{Q_0} \int_{t_0}^{t} \eta I_t dt \tag{4}$$

In Equation (4), S_{t_0} is the initial SOC value at time point t_0. By taking the SOC variation $\frac{1}{Q_0} \int_{t_0}^{t} \eta I_t dt$ into consideration, the

SOC value for the time point t is calculated. The state-space expression of the SO-ECM is established, as shown in Equation (5).

$$\begin{bmatrix} S_{t+\Delta t} \\ U_{p2,t+\Delta t} \\ U_{p2,t+\Delta t} \end{bmatrix} = \begin{bmatrix} 1 & 0 & 0 \\ 0 & exp\left(-\frac{\Delta t}{R_{p1}}\right) & 0 \\ 0 & 0 & exp\left(-\frac{\Delta t}{R_{p2}}\right) \end{bmatrix} \begin{bmatrix} S_t \\ U_{p1,t} \\ U_{p2,t} \end{bmatrix} + \begin{bmatrix} -\frac{\eta \Delta t}{Q_0} \\ R_{p1}\left[1-exp\left(-\frac{\Delta t}{R_{p1}C_{p1}}\right)\right] \\ R_{p2}\left[1-exp\left(-\frac{\Delta t}{R_{p2}C_{p2}}\right)\right] \end{bmatrix} I_t + \begin{bmatrix} w_{1,t} \\ w_{2,t} \\ w_{3,t} \end{bmatrix} \tag{5}$$

In Equation (5), the state-space variable is described by the matrix $X_t = [S_t, U_{p1}, t, U_{p2}, t]^T$ and the control-input variable is I_t.

The observation equation based on the SO-ECM is established, as shown in Equation (6).

$$U_t = f(S_t) - I_t R_0 - U_{p1,t} - U_{p2,t} + v_t \tag{6}$$

In Equation (6), the observation equation is obtained by real-time prediction and correction updates. Taking the observation

variable as $y_t = U_t$, the process noise $w_t = [w_{1,t}, w_{2,t}, w_{3,t}]^T$ with a covariance matrix Q is obtained. The iterative calculation

process is designed accordingly, as shown in Equation (7).

$$\begin{cases} [U_{p1}(t) - U_{p1}(t-1)]/T = -U_{p1}(t)/R_{p1}C_{p1} + I(t)/C_{p1} \\ [U_{p1}(t-1) - U_{p1}(t-2)]/T = -U_{p1}(t-1)/R_{p1}C_{p1} + I(t-1)/C_{p1} \\ [U_{p2}(t) - U_{p2}(t-1)]/T = -U_{p2}(t)/R_{p2}C_{p2} + I(t)/C_{p2} \\ [U_{p2}(t-1) - U_{p2}(t-2)]/T = -U_{p2}(t-1)/R_{p2}C_{p2} + I(t-1)/C_{p2} \end{cases} \tag{7}$$

In Equation (7), t and $t-1$ are the dependent current and previous time points, respectively. Combining the parameters of CCV

and current, the iterative calculation equation is obtained, as shown in Equation (8).

$$U_L(t) = c_0 + c_1 U_L(t-1) + c_2 U_L(t-2) + c_3 I(t) + c_4 I(t-1) + c_5 I(t-2) \tag{8}$$

In Equation (8), t, $t-1$, and $t-2$ are dependent time points. The parameters are calculated from the values of the two previous

time points to reduce the computational cost of the iterations. The value of the parameter R_0 is obtained, as shown in Equation (9).

$$R_0 = c_2/c_5 \tag{9}$$

In Equation (9), the internal ohmic resistance is obtained by the mathematical calculation of the coefficients of c_2 and c_5. Then,

the electrochemical polarization resistance is calculated, as shown in Equation (10).

$$R_{p1} = \frac{\left[-\tau_{p1}\frac{c_3 + c_4 + c_5}{1 - c_1 - c_2} + R_0\frac{c_1 + 2c_2}{1 - c_1 - c_2}T - R_0\tau_{p1} - \frac{c_4 + 2c_5}{1 - c_1 - c_2}T\right]}{\tau_1 - \tau_2} \tag{10}$$

In Equation (10), the R_{p1} is calculated by the coefficients and the time components. Combining R_0 and R_{p1}, the concentration polarization resistance R_{p2} is obtained, as shown in Equation (11).

$$R_{p2} = -\tau_1\frac{c_3 + c_4 + c_5}{1 - c_1 - c_2} - R_0 - R_{p1} \tag{11}$$

In Equation (11), according to the calculated value of R_{p1} at each SOC level and the mathematical relationship between the two RC circuits, the expressions for the electrochemical and concentration polarization capacitance are obtained, as shown in Equation (12).

$$\begin{cases} C_{p1} = \tau_1/R_{p1} \\ C_{p2} = \tau_2/R_{p2} \end{cases} \tag{12}$$

In Equation (12), the electrochemical and concentration polarization capacitance C_{p1} and C_{p2} are adjusted by the time constants and resistance. Then, the functional relationship between OCV and SOC is obtained by the logarithmic calculation, as shown in Equation (13).

$$U_{OC}(t) = K_0 + k_1 ln[S(t)] + k_2 ln[1 - S(t)] \tag{13}$$

In Equation (13), the functional relationship between the modeling coefficients is obtained to calculate the parameters, as shown in Equation (14).

$$\begin{cases} G(t) = P(t-1)\varphi(t)[I_{n_p} + \varphi^T(n_p, t)P(t-1)\varphi(n_p, t)]^{-1} \\ P(t) = P(t-1) - G(t)\varphi^T(t)P(t-1) \\ \hat{\theta}(t) = \hat{\theta}(t-1) + G(t)[Y(t) - \varphi^T(t)\hat{\theta}(t-1)] \end{cases} \tag{14}$$

In Equation (14), the observation noise is initialized with the covariance matrix R to obtain the coefficient matrices of the state-space model, as shown in Equation (15).

$$\begin{cases} A_t = \begin{bmatrix} 1 & 0 & 0 \\ 0 & exp[-\Delta t/(R_{p1}C_{p1})] & 0 \\ 0 & 0 & exp[-\Delta t/(R_{p2}C_{p2})] \end{bmatrix} \\ B_t = \begin{bmatrix} -\eta\Delta t/Q_n \\ R_{p1}(1 - exp[-\Delta t/(R_{p1}C_{p1})]) \\ R_{p2}(1 - exp[-\Delta t/(R_{p2}C_{p2})]) \end{bmatrix} \\ C_t = [\partial F_{(st)}/\partial S_t|_{S_t = S_t^-}, -1 \quad -1 \quad -1] \end{cases} \tag{15}$$

In Equation (15), A_t is the state transition matrix, B_t is the control-input matrix, and C_t is the measurement matrix of the system. η is the coulombic efficiency, which is defined as 1 in this study, and Q_n is the nominal capacity of the lithium-ion battery.

The internal electrochemical reaction does not stop immediately after the discharge, and the external performance is that the terminal voltage rises rapidly. Then, it gradually tends to a stable value, which is the rebound characteristic of lithium-ion batteries,
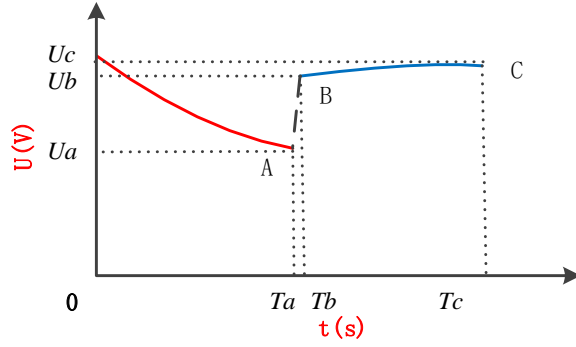
as shown in Figure 2.

Figure 2. Rebound characteristics of lithium-ion batteries

In Figure 2, point A indicates the time point when the discharge ends. The point B indicates the next time after the battery discharge ends. The point C indicates that the battery is stational. From the voltage variation, it can be observed that the rebound of lithium-ion batteries mainly includes the rapid rising stage from A to B and the slow rising stage from B to C. The rapid rising in voltage from A to B is mainly due to the increase in the ohmic internal resistance, and the slow rising stage from B to C is due to the internal polarization characteristics. The working characteristics of the SO-ECM are consistent with the rebound characteristics of lithium-ion batteries, so the parameters are identified by the voltage and current data of the battery in the rebound stage. After the discharge, the SO-ECM has zero input response, and the voltage variation with time is obtained, as shown in Equation (16).

$$U(t) = U(0)e^{-\frac{t}{RC}}; U_{p1}(0) = I(t)R_{p1}; U_{p2}(0) = I(t)R_{p2} \tag{16}$$

In Equation (16), the mathematical relationship between the electrical parameters for the zero-state response is expressed. According to Kirchoff's circuit law, the terminal voltage from B to C at any time point is obtained, as shown in Equation (17).

$$U_L(t) = U_{OC} - U_{p1}(t) - U_{p2}(t) = U_{OC} - U_{p1}(0)e^{-\frac{t}{R_{p1}C_{p1}}} - U_{p2}(0)e^{-\frac{t}{R_{p2}C_{p2}}}$$
$$= U_{OC} - I(t)R_{p1}e^{-\frac{t}{\tau_1}} - I(t)R_{p2}e^{-\frac{t}{\tau_2}} \tag{17}$$

In Equation (17), τ_1 and τ_2 are the curve fitting coefficients, so that the calculation procedure and relationship are obtained, as shown in Equation (18).

$$\tau_1 = R_{p1}C_{p1}; \tau_2 = R_{p2}C_{p2}; \tau_1 > \tau_2 \tag{18}$$

In Equation (18), the calculation procedure is designed for the battery's parameters based on the curve fitting coefficients. The observation equation towards time in the rebound stage is fitted, as shown in Equation (19).

$$y = k_0 - k_1 e^{-b_1 t} - k_2 e^{-b_2 t} \tag{19}$$

In Equation (19), the general expression of the observation equation is obtained. According to the experimental data, the values

of k_0, k_1, k_2, b_1, and b_2 are obtained by the curve fitting method. Then, the model parameters are calculated accordingly, as shown in Equation (20).

$$\begin{cases} R_0 = \dfrac{\Delta U_{AB}}{I}; R_{p1} = \dfrac{k_1}{I}; \ R_{p2} = \dfrac{k_2}{I}; \\ \quad C_{p1} = \dfrac{b_1}{R_{p1}}; C_{p2} = \dfrac{b_2}{R_{p2}} \end{cases} \tag{20}$$

In Equation (20), after obtaining the main coefficient parameters, the iterative calculation of the proposed FC-AKF algorithm is realized with effective prediction and correction updates.

2.3.   Feedback correction-adaptive Kalman filter

In the prediction process, the improved FC-AKF method continuously corrects the SOC value through the error covariance correction and system noise update in real-time for accurate prediction. The main purpose is to determine the initial and updated state parameters for the next time point with an updated error covariance matrix. Then, the parameter value is calculated based on the weight update of the Kalman gain. For the next time point calculation, the state and error covariance prediction is realized through the iterative prediction and correction of the mean covariance error and covariance that are updated continuously, as shown in Figure 3.
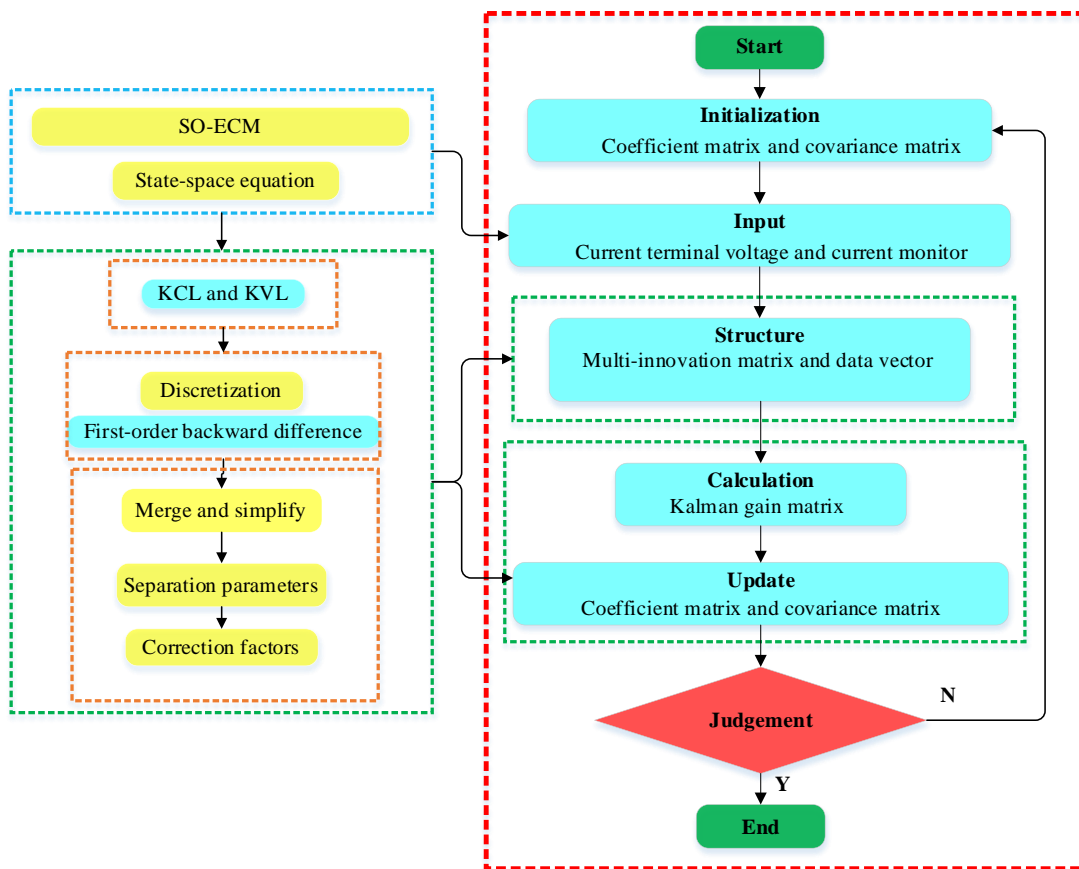

Figure 3. Flowchart of the feedback correction-adaptive Kalman filter

In Figure 3, judging whether the system dynamics are changed by filtering constantly, the model parameters are predicted and corrected by considering the statistical noise characteristics to reduce the prediction error. The predicted state value $\hat{x}_t$, noise variance $\hat{q}_{t+1}$, and u_t are predicted in real-time with the measured data to realize the state prediction, as shown in Equation (21).

$$\hat{q}_{t+1} = \frac{1}{t+1} G \sum_{t=0}^{k} (\hat{x}_{t+1} - A\hat{x}_t - Bu_t) \tag{21}$$

The noises' covariance matrices Q_t and R_t are updated in real-time to improve the prediction accuracy and robustness, as shown in Equation (22).

$$\hat{Q}_{t+1} = \frac{1}{t+1} G \sum_{t=0}^{k} (L_{t+1}\tilde{y}_{t+1}y_{t+1}{}^{T}L_{t+1} + \tilde{P}_{t+1} - AP_{t+1}A^{T})G^{T} \tag{22}$$

In Equation (22), the mean value of the process noise w_t and the measurement noise v_t is zero. The calculation of the correlation parameter designed for the system noise correction, as shown in Equation (23).

$$\hat{r}_{t+1} = \frac{1}{t+1} \sum_{t=0}^{k} (y_{t+1} - C\hat{x}_{t+1|t}) \tag{23}$$

In Equation (23), the parameter identification and state prediction are combined organically. The noise statistical characteristic prediction is realized by the iterative calculation, as shown in Equation (24).

$$\hat{R}_{t+1} = \frac{1}{t+1} \sum_{t=0}^{k} (\tilde{y}_{t+1} \tilde{y}^{T}{}_{t+1} - CP_{t+1|t}C^{T}) \tag{24}$$

In Equation (24), the statistical quantity is obtained towards the prediction factors. y_{t+1} is the corresponding state observation signal. u_t is the system input quantity. A_t is the state transition matrix, B_t is the control matrix. C_t is the observation matrix. The coefficient G is obtained by $G = (\Gamma\Gamma^{T})\Gamma^{T}$, in which Γ is used as the driving matrix noise. These equations are arithmetic averages, and the weighting coefficients of each term are considered. In the time-varying battery systems, recent data has a great impact on the state prediction, so the exponential weighting treatment is adopted to improve the prediction effect. Consequently, each formula is multiplied by the exponential weighting coefficient β, as shown in Equation (25).

$$\beta_i = \beta_{i-1}b, \left(0 < b < 1, \sum_{t=0}^{k} \beta_i = 1\right) \tag{25}$$

In Equation (25), as for the iterative calculation of the exponential weighting coefficient β, the expression is further obtained by conducting the coefficient calculation, as shown in Equation (26).

$$\beta_i = d_t b^i, \left(d_k = \frac{1-b}{1-b^{t+1}}, i = 0,1,2,3 \dots, k\right) \tag{26}$$

In Equation (26), b is the forgetting factor. By substituting each item $(k+1)^{-1}$ with the original predicted coefficient β_{t-1}, the

noise prediction requirements of the improved time-varying system are obtained. The specific steps are designed as follows:

(1) Initialization

The initial value of the system state and error covariance matrix is designed, as shown in Equation (27).

$$\hat{x}_0 = E[X_0], P_0 = E[(X_0 - \hat{x}_0(X_0 - \hat{x}_0)^T] \tag{27}$$

(2) Error covariance correction

The state and error covariance matrices at the time point $k + 1$ are calculated, as shown in Equation (28).

$$\begin{cases} \hat{X}_{t+1|t} = A\hat{X}_t + Bu_t + \Gamma\hat{q}_t \\ P_{t+1|t} = AP_tA^T + \Gamma\hat{Q}_t\Gamma^T \end{cases} \tag{28}$$

(3) Kalman gain calculation

According to the error covariance obtained in the previous step, the Kalman gain is calculated in real-time, as shown in Equation (29).

$$L_t = P_{t+1|t}C^T(CP_{t+1|t}C^T + \hat{R}_t)^{-1} \tag{29}$$

(4) Error covariance update

According to the observation value of $\bar{y}_{t+1}$ in the battery system, the state prediction and error covariance matrix are updated for the time point $t + 1$, as shown in Equation (30).

$$\begin{cases} \hat{X}_{t+1} = \hat{X}_{t+1|t} + L_t\bar{y}_{t+1} \\ P_{t+1|t} = (E - L_tC)P_{t+1|t} \end{cases} \tag{30}$$

In Equation (30), E is an identity matrix. Consequently, the core parameters are updated accordingly, including $\hat{r}_t$, $\hat{q}_t$, $\hat{Q}_t$, and $\hat{R}_t$. Then, the procedure returns to step (1) and continues to carry out the iterative calculation. Subsequently, the unscented transformation is also conducted for the output voltage traction to realize the real-time state prediction with the update, as shown in Equation (31).

$$\begin{cases} x_{t|t-1}^- = f\left(x_{t|t-1}^-\right), \bar{x}_t = \sum_{t=0}^{2L} \omega_i^m x_{t|t-1}^i \\ p_{t|t-1} = \sum_{t=0}^{2L} \omega_i^c\left(x_{t|t-1}^i - \bar{x}\right)\left(x_{t|t-1}^i - \bar{x}\right)^T + Q_t \\ y_{t|t-1}^i = g\left(x_{t|t-1}^i\right), \bar{y}_t = \sum_{t=0}^{2L} \omega_i^m\left[g\left(x_{t|t-1}^i\right) + v_{t-1}^i\right] = \sum_{t=0}^{2L} \omega_i^m y_{t|t-1}^i \end{cases} \tag{31}$$

In Equation (31), $x_{t|t-1}^i$ is the predicted value obtained from the time point $t - 1$. Subsequently, the accurate iterative calculation is also realized for real-time state monitoring, which has a significant influence on the battery's safety. The operating characteristics are analyzed by integrating various calculation procedures to realize real-time state monitoring. Then, the measured and updated parameter value can be obtained, as shown in Equation (32).

$$\begin{cases} p_{t|t-1} = \sum_{t=0}^{2L} \omega_i^c \left(x_{t|t-1}^i - \bar{x} \right) \left(x_{t|t-1}^i - \bar{x} \right)^T + Q_t \\ p_{\bar{x}\bar{y},t} = \sum_{t=0}^{2L} \omega_i^c \left(x_{t|t-1}^i - \bar{x} \right) \left(y_{t|t-1}^i - \bar{y} \right)^T \\ K = p_{\bar{x}\bar{y},t} p_{\bar{y},t}^{-1}, \bar{x}_t = \bar{x}_{t-1} + K(y_t - \bar{y}_{t-1}) \\ p_{t|t} = p_{t|t-1} - K p_{\bar{x}\bar{y},t-1} K^T \end{cases} \tag{32}$$

By repeating these four calculation steps, the optimal state prediction is realized, in which the state parameter X_t is obtained at the time point t by the given initial state variables of X_0 and P_0. According to the state value at the time point $t - 1$, the observed value is predicted by taking it as an input. The built-in model of the data performance is conducted and combined with the working condition influence, making the established prediction model realization effective. It has many advantages, including quick convergence speed and effective tracking performance. The prediction error is reduced effectively with high accuracy advantages in the iterative calculation process. According to mathematical modeling effect analysis, the calculation expression is obtained as shown in Equation (33).

$$\begin{cases} E(t) = U_L(t) + U_{p1}(t) + U_{p2}(t) + I(t)R_0 \\ \dot{U}(t) = \dfrac{I(t)}{C_{p1} + C_{p2}} - \dfrac{U_{p1}(t)}{(R_{p1}C_{p1})} - \dfrac{U_{p2}(t)}{(R_{p2}C_{p2})} \end{cases} \tag{33}$$

In Equation (33), $E(t)$ is the electromotive force of the power supply. The relationship between $E(t)$ and the state parameter $S(t)$ is described by the nonlinear functional description. $U_L(t)$ is terminal voltage, $U_{p1}(t)$ and $U_{p2}(t)$ are the polarization voltage factors, and R_0 is internal ohmic resistance.

Then, $S(t)$ is obtained by combining the Ah integral method and other influencing factors. $S(t)$ is the state parameter and $U_L(t)$ is the observed quantity. As the prediction process is a discrete calculation process, the relationship between $S(t + 1)$ and $S(t)$ is obtained after discretization, as shown in Equation (34).

$$S(t) = S(t_0) - \int_0^t \frac{\eta I(t)}{Q} dt \Rightarrow S(t + 1) = S(t) - \frac{\Delta T \times I(t)}{Q} + v(t) \tag{34}$$

In Equation (34), the point sets of mean and covariance are calculated after the transformation, and an asymmetric sampling strategy is introduced into the calculation process.

The dimension of the state variable x is n to calculate the mean and covariance matrix with the observed variable. Finally, the sampling points are obtained with the nonlinear observing function. $S(t + 1)$ and $S(t)$ represent state parameters at the time point $t + 1$ and t. Q is the quantity of electricity and ΔT is the unit parameter as the sampling period. Taking $v(t)$ as the observation noise, the observation equation is obtained, as shown in Equation (35).

$$U(t) = f[S(t)] - R_0 I(t) - U_p(t) + v(t) \tag{35}$$

In Equation (35), the electromotive force of the power supply at the time point t is characterized by $U(t)$. $f[S(t)]$ represents

13

the non-linear relationship between OCV and SOC. R_0 is the internal ohmic resistance. $I(t)$ represents the current measured at the time point t. $U_p(t)$ is the polarization voltage at the time point t and $v(t)$ is the measurement noise.

2.4. Iterative feedback correction strategies

For the nonlinear battery's state prediction, the proposed FC-AKF algorithm conducts the forced linearization. It carries out the probability density prediction of the state variables with an accurate feedback correction strategy to obtain the optimal solution. The transformation depends on the acquisition of sampling points, the determination of corresponding weights is initialed accordingly. The coefficient parameters are generally taken as $\beta \geq 0$ and $0.2 \leq \alpha \leq 1$. A scaling factor, λ, is used to generally satisfy the mathematical relationship functions. The sampling points are transferred nonlinearly with the functional relationship, as shown in Equation (36).

$$\begin{cases} \kappa = 3 - n, \lambda = \alpha^2(n + \kappa) - n \\ \quad y^i = f(x^i), i = 0 \sim 2n \end{cases} \tag{36}$$

In Equation (36), the unscented transformation is introduced to solve the nonlinear battery state prediction problem, which is an important part of the energy management strategy. It is realized according to the statistical parameter features, in which a certain sampling treatment is conducted for the corresponding finite number of sampling data points. The mean and covariance of these data points are the same as the original state, which is then introduced into the nonlinear transformation function, obtaining the corresponding data values. It uses the state and observation equations to realize the optimal state prediction of minimum variance by observing the input-output parameters. The mean and covariance are calculated after transformation, as shown in Equation (37).

$$\hat{y} = \sum_{t=0}^{2n} \omega_t f(x_t) \Rightarrow P_y = \sum_{t=0}^{2n} \omega_t [f(x_t) - \hat{y}] [f(x_t) - \hat{y}]^T \tag{37}$$

In Equation (37), the implementation process is divided into two stages, including prediction and update. According to the symmetric sampling strategy, sigma points are used as the sampling data, which needs to meet the same mean and covariance conditions. Considering the SO-ECM and the operating conditions, SOC is used as the state variable, and U_0 is taken as the observation variable. The established state-space expression is obtained, as shown in Equation (38).

$$\begin{cases} S_{t+1} = S_t - I_t \dfrac{\Delta t}{Q_n + w_{t+1}} \\ U_{0,t+1} = f(S_{t+1}) - U_0 - U_1 + v_{t+1} \end{cases} \tag{38}$$

In Equation (38), the state value at the time point t is used to predict the SOC value for the next time point $t + 1$. Δt is the sampling interval. Q_n is the rated capacity, which is calibrated. I_t is the current at the time point t, assuming charging is positive and discharging is negative. $U_{OC,t+1} = f(S_{t+1})$ is the relationship function between the OCV and SOC. w_{t+1} and v_{t+1} are the process and measurement noises, respectively. Meanwhile, the real-time prediction error correction is conducted between the measured variable and prediction value. Finally, the optimal prediction of state variables is realized. The predicted value of the

14

state variable at the time point $t + 1$ is obtained accordingly, as shown in Equation (39).

$$x_{t+1|t}^i = f\left(x_t^i, u_t\right) \Rightarrow \hat{x}_{t+1|t} = \sum_{t=0}^{2L} \omega_m^i \, x_{t+1|t}^i \tag{39}$$

In Equation (39), the data sequence is described with the sampling points obtained by conducting the unscented transformation for the time point $t = 1, 2, 3, \ldots, 2n + 1$. Combined with the prediction equation, the sampling points are obtained by taking u_t as the input factor. The weighted sum is used to obtain the mean value. Similarly, the error variance matrix at the time point $t + 1$ is calculated, as shown in Equation (40).

$$P_{x,t+1|t} = \sum_{t=0}^{2L} \omega_c^i \left[x_{t+1|t}^i - \hat{x}_{t+1|t}\right] \left[x_{t+1|t}^i - \hat{x}_{t+1|t}\right]^T + Q_{t+1} \tag{40}$$

In Equation (40), the predicted state parameter, and the covariance are obtained by updating the sampling sigma data points. The predictive value for the time point $t + 1$ is obtained to realize the update of the sampling points. The observation at each sampling time point is the expected value. The predicted weighted terminal voltage at the time point $t + 1$ is calculated by considering the mean measured value, as shown in Equation (41).

$$y_{t+1|t}^i = h\left(x_{t+1|t}^i, u_{t+1}\right) \Rightarrow \hat{y}_{t+1|t} = \sum_{t=0}^{2n} \omega_m^i \, y_{t+1|t}^i \tag{41}$$

In Equation (41), the state variable S_t at the time point t is known in advance with the error covariance matrix $P_{xy,t+1}$, to realize the specific iterative calculation. At the prediction stage, the sigma points are transferred by the state equation. Then, the predicted data points are obtained, which are modified recursively by the real-time Kalman gain correction. The measured covariance matrix can be obtained for the calculated state quantity at the time point $t + 1$ in the measurement-correction step, as shown in Equation (42).

$$\begin{cases} P_{yy,t+1} = \displaystyle\sum_{t=0}^{2L} \omega_c^i \left[y_{t+1|t}^i - \hat{y}_{t+1|t}\right] \left[y_{t+1|t}^i - \hat{y}_{t+1|t}\right]^T + R_{t+1} \\[4mm] P_{xy,t+1} = \displaystyle\sum_{t=0}^{2L} \omega_c^i \left[x_{t+1|t}^i - \hat{x}_{t+1|t}\right] \left[y_{t+1|t}^i - \hat{y}_{t+1|t}\right]^T \end{cases} \tag{42}$$

In Equation (42), the predicted mean value is updated in the state variable and error update module, which is conducted with the corresponding error covariance based on the real-time observed data. Then, the Kalman gain is obtained for the next iterative calculation step. The Kalman gain is used as the correction parameter to forecast the observation quantity. The updated state variable calculation is then realized with the update of the error variance matrix, as shown in Equation (43).

$$\begin{cases} \hat{x}_{t+1|t} = \hat{x}_{t+1|t} + K_{t+1}\left(y_{t+1} - \hat{y}_{t+1|t}\right), K_{t+1} = \dfrac{P_{xy,t+1}}{P_{yy,t+1}} \\[4mm] P_{x,t+1|t+1} = P_{x,t+1|t} - K_{t+1} P_{xy,t+1} K_{t+1}^T \end{cases} \tag{43}$$

In Equation (43), the nonlinear transformation is investigated to calculate the real-time data points with the weighted summation with the average value of the state prediction. Then, the sigma points are updated by introducing the correction steps into the observing process with the forecast and unscented transformation.

3.   Experimental Analysis

The whole-life-cycle experimental test is designed and conducted to verify the effect of the proposed SO-ECM and FC-AKF algorithm. The parameter identification is realized with the dataset from the HPPC test and dynamic working condition tests for the prediction effect verification.

3.1.   Varying current-temperature testing

Various working condition tests are performed by the comprehensive testing system, in which the battery performance is obtained for the lithium-ion batteries. The detailed platform design, procedure, and experimental results are shown in https://www.researchgate.net/project/Battery-life-test. Consequently, the internal working state of lithium-ion batteries is analyzed, and the parameter value is obtained through calculation. Batteries are connected to the system channel, and the experimental step is designed according to the testing requirement. After the experimental equipment is set up, the real-time charge and discharge data for the lithium-ion battery are sampled by the data signal measurement.

The intermittent discharge is conducted using a current rate of 1 C, according to the relationship between the discharge rate and the number of coordinates required set of each discharge loop time. The discharge period is 6 min every time, and the internal chemical state stability of the OCV discharge is shelved for 1 h to get the OCV-SOC relationship. The voltage variation with the charging and discharging conditions reflects the battery's dynamic characteristics during operation. The key parameters of the SO-ECM are determined by the HPPC test. The ohmic resistance value is measured by the instantaneous dynamic terminal voltage change from the beginning to the end of the charge and discharge processes. The internal polarization resistance and capacitance are detected and obtained through the slow change of the terminal voltage. The specific experimental steps for the HPPC experiment are designed as follows:

First, the lithium-ion battery is charged with a constant current of 0.3 C till the cut-off voltage. When the terminal voltage is reached, the charging process is continued with this constant voltage. When the current rate decreases to 0.05 C, the battery is fully charged. The battery is shelved for 1 h, which is then discharged with a current rate of 1 C for 10 s with a shelved for 40 s to stabilize the battery. Then, the battery is charged at a current rate of 0.75 C for 10 s. In the cycling test, the battery pulse power at equally spaced SOC levels, which equally vary from 1.0 to 0.1. The voltage variation results of the whole-life-cycle test under the HPPC working condition are shown in Figure 4.
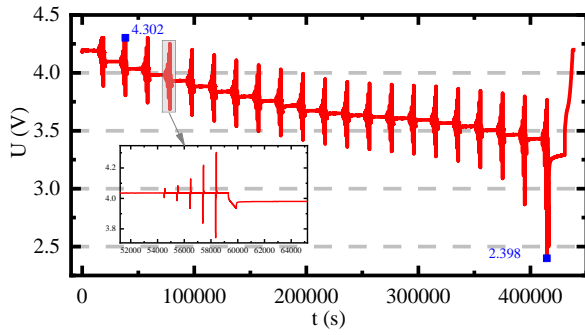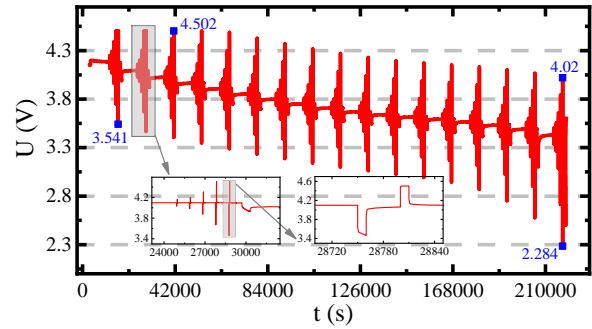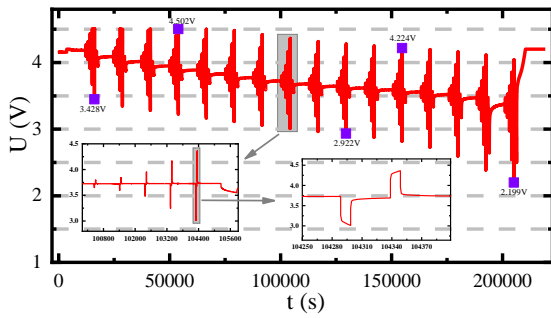
(a) OCV variation for 20 cycles at SOC = 1.0 under 25 □
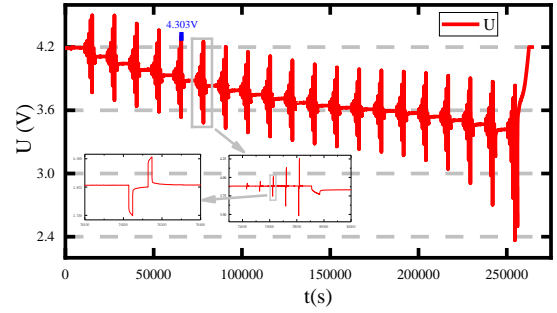
(b) OCV variation for 20 cycles at SOC = 1.0 under 25 □
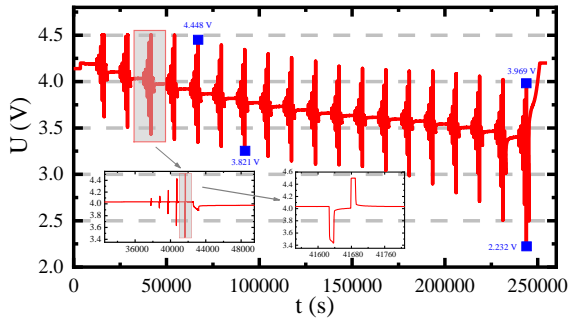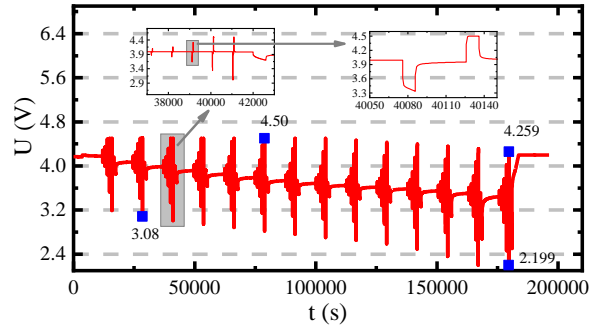

(c) OCV variation for 20 cycles at SOC = 0.90 under 25 □

(d) OCV variation for 20 cycles at SOC = 0.85 under 25 □

(e) OCV variation for 20 cycles at SOC = 0.80 under 25 □

(f) OCV variation for 20 cycles at SOC = 0.75 under 25 □

Figure 4. OCV variation of the whole-life-cycle test under the HPPC working condition

In Figure 4, the SOC varies from 100% to 75%. The battery is shelved for one hour between each adjacent pulse test, restoring the battery to electrochemical and thermal equilibrium. The parameters are identified by the established nonlinear state-space equation by the SO-ECM for different SOC levels. The internal resistance, polarization capacitance, and polarization resistance are obtained corresponding to the SOC levels from 1.0 to 0.1, as shown in Table 1.

Table 1. Values of the parameters for the SO-ECM

SOC (1)	U_{OC} (V)	R_0 (mΩ)	R_{p1} (mΩ)	R_{p2} (mΩ)	C_{p1} (F)	C_{p2} (F)
1.0	4.1840	0.001092857	0.000444000	0.000043286	31846.8468	21709.2409
0.9	4.0513	0.001107143	0.000496143	0.000049300	28761.8773	19083.1643
0.8	3.9360	0.001102857	0.000628143	0.000053857	29260.8597	17136.0743
0.7	3.8309	0.001111429	0.000554857	0.000041943	25682.2863	17964.9183
0.6	3.7366	0.001124286	0.000507429	0.000040700	27767.4550	18088.4521
0.5	3.6511	0.001132857	0.000452286	0.000035329	39289.3241	26366.7610
0.4	3.6163	0.001147143	0.000381429	0.000028214	36127.3408	28988.8608
0.3	3.5900	0.001151429	0.000365571	0.000027971	32797.9680	20327.8856
0.2	3.5367	0.001151429	0.000415857	0.000032529	29264.8574	25485.2877
0.1	3.4545	0.001187143	0.000516000	0.000047757	22267.4419	11880.9453

In Table 1, the battery voltage at the end of each discharge is used as the OCV value corresponding to the various SOC levels. These discrete points are extracted from the experimental data to obtain the OCV-SOC relationship curve. According to the experimental analysis of the HPPC test, the voltage and current variation curves for the dynamic response characteristics of SOC decreased from 1 to 0.1. The various internal parameters of the battery are obtained for different SOC levels during operation. These parameters are used to verify the accuracy and robustness of the proposed SO-ECM.

3.2. Whole-life-cycle test under the BBDST working condition

A lithium-ion battery (HTCNR18650-2200mAh-3.6V) is used for the experiment. The whole-life-cycle experimental procedure is designed, as shown in Figure 5.
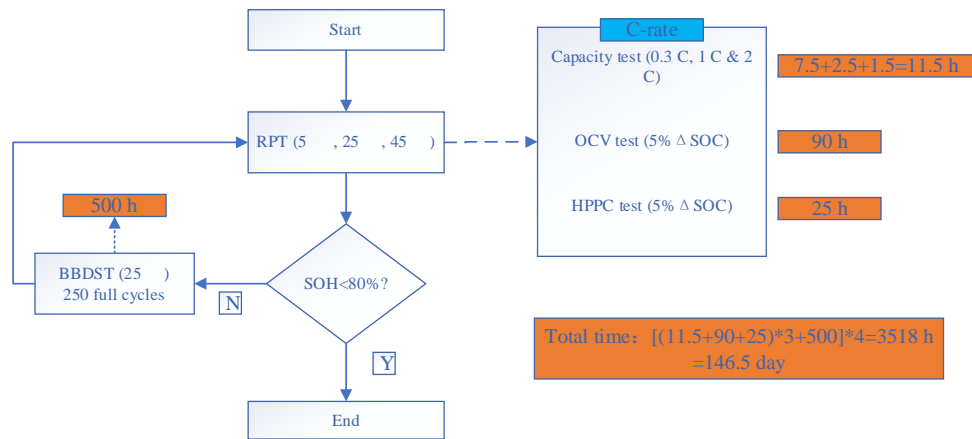

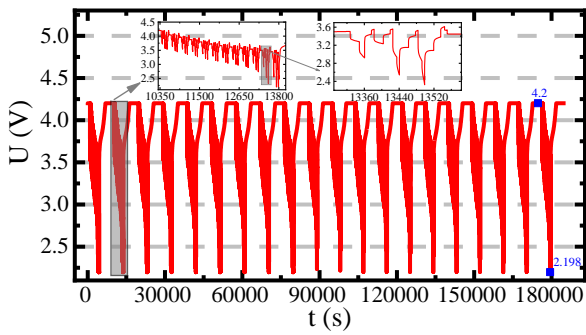Figure 5. Flowchart of the whole-life-cycle test under the BBDST working condition

In Figure 5, the experimental test procedure for the various test is presented based on the current state of the lithium-ion battery for the capacity, OCV, and HPPC tests. The voltage variation results of the whole-life-cycle test under the BBDST working condition are shown in Figure 6.
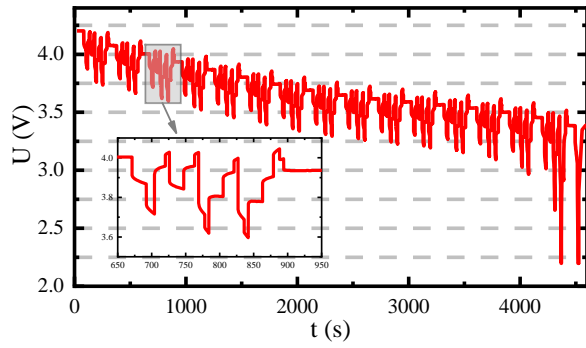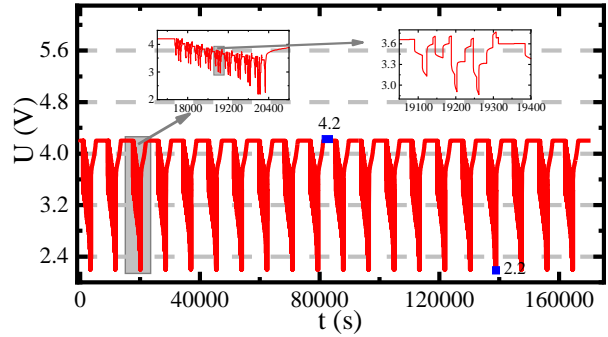
(a) Voltage variation for 20 cycles at SOC < 0.1
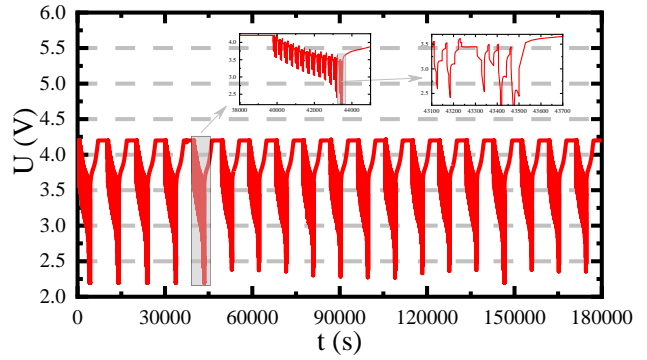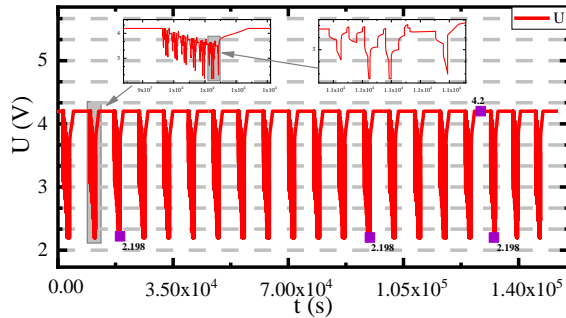

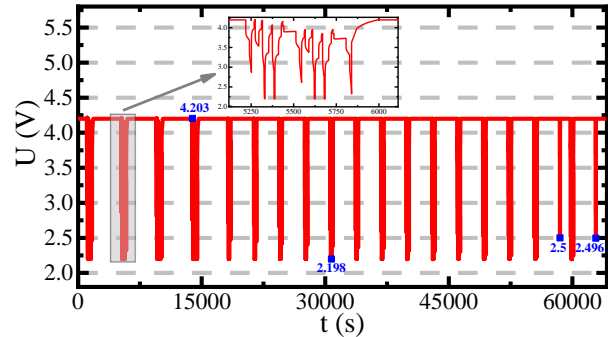(b) Voltage variation for 20 cycles at SOC = 0.1

(c) Voltage variation for 20 cycles at SOC = 0.2

(d) Voltage variation for 20 cycles at SOC = 0.3

(e) Voltage variation for 20 cycles at SOC = 0.4

(f) Voltage variation for 20 cycles at SOC = 0.5

Figure 6. Voltage variation of the whole-life-cycle test under the BBDST working condition

In Figure 6, based on experimental results, the mathematical model for the SO-ECM is established. Then, the iterative calculation is programmed in the *S*-function to realize the accurate prediction. Finally, the feasibility and accuracy of the proposed state prediction algorithm are verified through verification experiments under complex working conditions.

3.3. Long-term SOC prediction under the BBDST working condition

The SOC is predicted under the complex BBDST working to investigate the accuracy and robustness of the proposed FC-

AKF algorithm over long-term battery life. The SOC prediction and error results are obtained, as shown in Figure 7.

(a) SOC prediction result
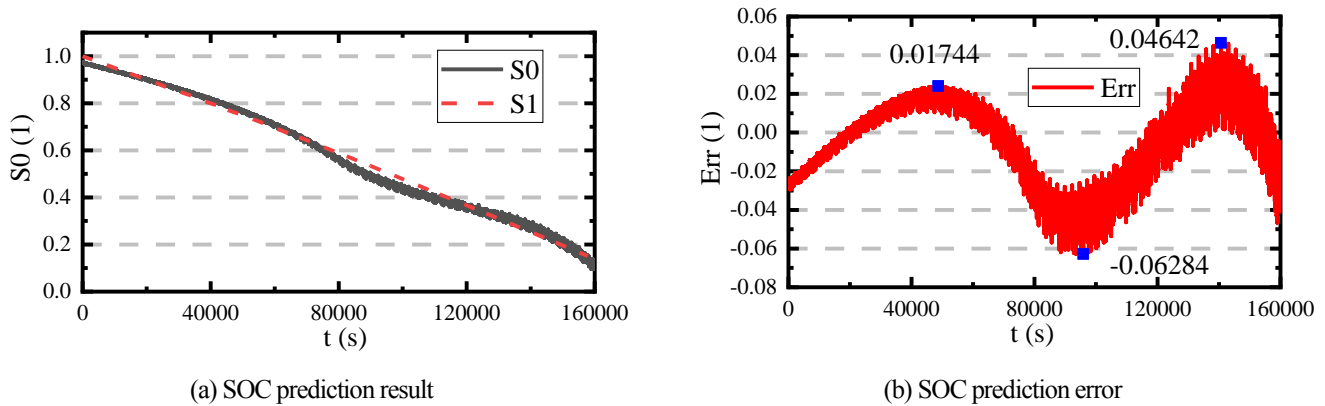
(b) SOC prediction error

Figure 7. State prediction and error results under the BBDST working condition

In Figure 7(a), the SOC predicted is compared with the actual SOC of the battery system over long-term battery life. $S0$ is the actual SOC, and $S1$ is the predicted SOC by the proposed FC-AKF. Also, Figure 7(b) is the SOC prediction error. The results show that the maximum error is 6.284% when the prediction is carried out over the long-term life of the battery, which shows the robustness of the proposed FC-AKF algorithm. Comparative SOC prediction under the dynamic stress test working condition

The accuracy of the proposed FC-AKF is verified under various experimental conditions to investigate the overall performance of the lithium-ion battery SOC prediction model. The constant current discharge experiment is performed on the prediction model. The constant current rate of 1 C is also used to verify the convergence effect of the proposed algorithm when the initial SOC value is not 1.0. The obtained voltage and current data are imported into the prediction model, which is used to predict the SOC under the dynamic stress test (DST) working condition. The battery parameters are obtained by the SO-ECM, including the capacity, current, and voltage during the charging and discharging processes. Also, the other parameters are internal parameters that have functional relationships as independent variables, changing with the SOC variation. After the experimental verification, the accuracy of the model is verified, and the parameters of the battery are introduced into the FC-AKF algorithm and compared the Ah integral method. The SOC prediction and error results are conducted under the DST working condition, as shown in Figure 8.

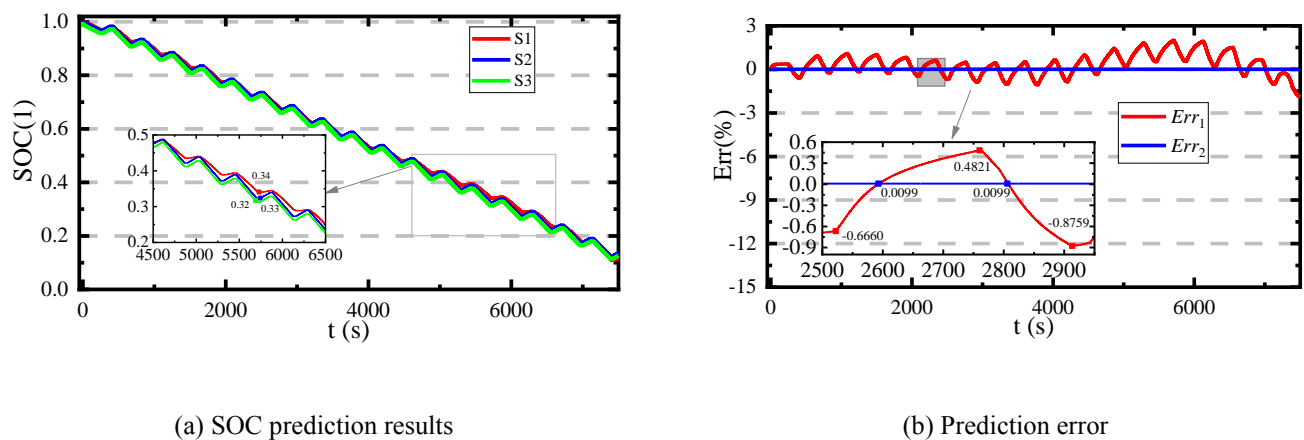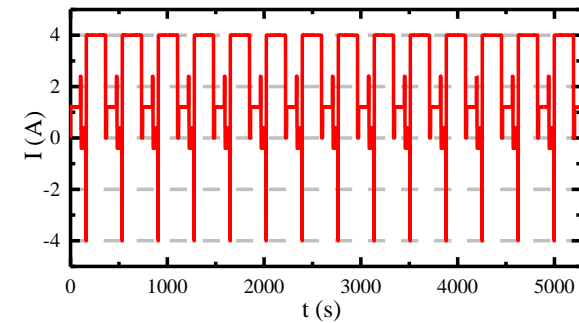(a) SOC prediction results

(b) Prediction error
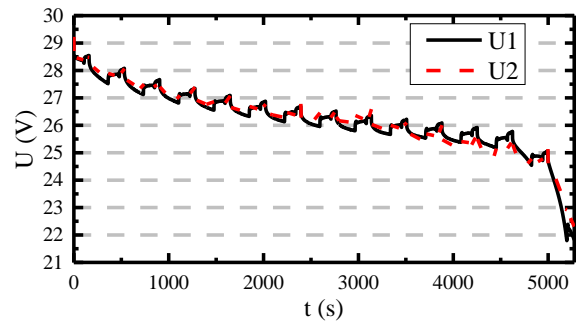
Figure 8. SOC prediction and error results

In Figure 8, the SOC is predicted under the DST working condition for a short-term battery life with the prediction error. In Figure 8 (a), $S1$ is the prediction made by the Ah integral method, $S2$ is the prediction made by the proposed FC-AKF method, and $S3$ is the actual SOC of the battery system. Also, in Figure 8(b), Err1 is the prediction error of the Ah integral method, and Err2 is the prediction error of the proposed FC-AKF method. The results show that the Ah integral method predicts a maximum error of 2.13%, while the FC-AKF predicts a maximum of 0.0099%. From the results, the Ah integration method cannot converge to track the actual SOC value, but the FC-AKF has a stable and robust prediction. As the prediction time increases, the larger the divergence of the prediction becomes, resulting in a large error, which is due to the accumulation of errors over time. Both the EKF and UKF algorithms track real SOC values and are stable at the end of the prediction.
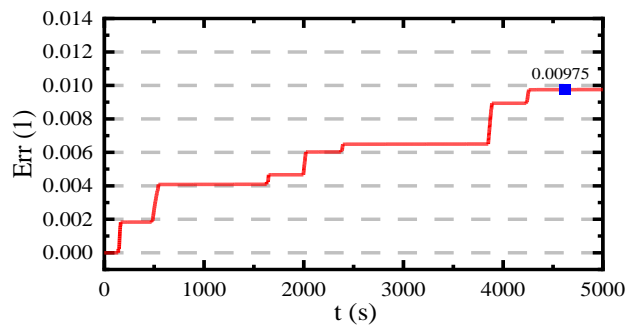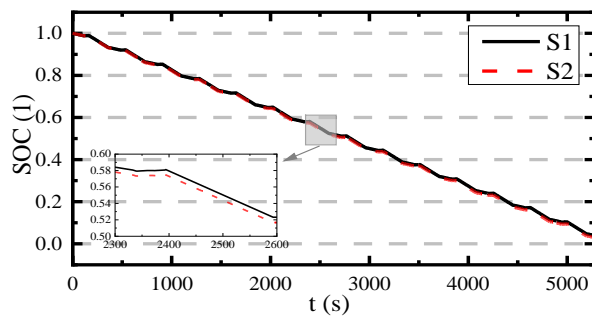
3.4. Packing CCV and SOC prediction

For the complex current variation experimental test, seven serially connected battery cells with a capacity of 2.20 Ah are used to further analyze the packing state prediction effect. The experimental test of the input current is conducted under complex packing power supply conditions. In the prediction process, the predicted initial value is 0.95 and the measured value is 1.00. The working current is output to the workspace at time intervals during the factor measurement process. The CCV and SOC prediction results are extracted, as shown in Figure 9.

(a) Pulse-power current variation

(b) Packing CCV tracking effect

(c) SOC prediction   (d) SOC prediction error

Figure 9. Packing CCV traction and SOC prediction results

In Figure 9(b), the predicted voltage of the SO-ECM tracks the CCV value under complex working conditions. The predicted voltage variation follows the measured voltage change accurately in each current mutation point of the overall model with the same changing trend. The relatively high-precision experimental verification is conducted to establish the SO-ECM with the maximum error of 0.08 V and an average error of 0.04 V. The experimental verification result shows that the SO-ECM works well even when the initial value is inaccurate.

In Figure 9(c), $S1$ is the actual SOC of the battery system, and $S2$ is the prediction made by the proposed FC-AKF method. The SO-ECM tracks the CCV value, and the proposed FC-AKF algorithm predicts the SOC value accurately under the complex working condition, in which the maximum error is 0.975% for the short-term prediction. The proposed FC-AKF algorithm also has a strong self-correcting ability, and the predicted curve converges to the actual curve within a limited sampling period. It verifies that it has good self-adaptive adjustment ability for the initial state error correction without the prediction accuracy declining. The proposed method is more effective in predicting the SOC of lithium-ion batteries. It is more computationally efficient, accurate, and robust than the Ah integral method used to compare in this paper due to its recursive update of the error covariance matrix, which ensures the reduction of the effects of noise in the prediction process.

4.   Conclusion

As core aspects of the battery's internal parameters, CCV and SOC prediction play an essential role in energy storage systems. After comparing with the traditional methods and combining existing conditions, the SO-ECM and FC-AKF methods are proposed and realized to achieve a high precision prediction. Taking the battery polarization into account, the two RC circuits of the established SO-ECM dynamically describe the dynamic characteristics of lithium-ion batteries. A transient charge-discharge process is used, which is a nonlinear low-order modeling method involving fewer parameters and higher precision effects. By comparing and analyzing the SOC values obtained by different prediction methods, it is observed that the error range of FC-AKF is smaller than that of the Ah integral method under the DST working conditions. The constructed SO-ECM tracks with a maximum error of 0.08 V and an average error of 0.04 V. Also, the proposed FC-AKF method promotes the accurate state co-prediction effect by 2.13% under the DST working condition and 0.975% under the BBDST working condition to improve the safety and longevity of lithium-ion batteries. Nowadays, the new energy application is more and more popular in the industry and our daily life, security management, and assurance are urgent for the lithium-ion battery system that is adaptive to various working conditions, so the proposed FC-AKF method will be embedded in the microprocessor to realize the realtime SOC prediction and the further health management based on the accurate and robust prediction results.

References

[1] Y. T. Liu *et al.*, "A Nonlinear Observer SOC Estimation Method Based on Electrochemical Model for Lithium-Ion Battery," (in English), *Ieee Transactions on Industry Applications,* vol. 57, no. 1, pp. 1094-1104, Jan 2021.

[2] E. P. M. Leiva, "Modeling of lithium-ion batteries is becoming viral: where to go?," (in English), *Journal Of Solid State Electrochemistry,* vol. 24, no. 9, pp. 2117-2120, Sep 2020.

[3] X. Lai *et al.*, "Mechanism, modeling, detection, and prevention of the internal short circuit in lithium-ion batteries: Recent advances and perspectives," (in English), *Energy Storage Materials,* vol. 35, pp. 470-499, Mar 2021.

[4] B. H. Liu *et al.*, "Quantifying and modeling of stress-driven short-circuits in lithium-ion batteries in electrified vehicles," (in English), *Journal Of Materials Chemistry A,* vol. 9, no. 11, pp. 7102-7113, Mar 21 2021.

[5] T. Z. Zhao, Y. J. Zheng, J. H. Liu, X. Zhou, Z. Y. Chu, and X. B. Han, "A study on half-cell equivalent circuit model of lithium-ion battery based on reference electrode," (in English), *International Journal Of Energy Research,* vol. 45, no. 3, pp. 4155-4169, Mar 10 2021.

[6] J. Khalfi, N. Boumaaz, A. Soulmani, and E. Laadissi, "Nonlinear Modeling of Lithium-Ion Battery Cells for Electric Vehicles using a Hammerstein-Wiener Model," (in English), *Journal Of Electrical Engineering & Technology,* vol. 16, no. 2, pp. 659-669, Mar 2021.

[7] S. R. Hashemi, A. B. Baghbadorani, R. Esmaeeli, A. Mahajan, and S. Farhad, "Machine learning-based model for lithium-ion batteries in BMS of electric/hybrid electric aircraft," (in English), *International Journal Of Energy Research,* vol. 45, no. 4, pp. 5747-5765, Mar 25 2021.

[8] W. Zhou, R. J. Huang, K. Liu, and W. G. Zhang, "A novel interval-based approach for quantifying practical parameter identifiability of a lithium-ion battery model," (in English), *International Journal Of Energy Research,* vol. 44, no. 5, pp. 3558-3573, Apr 2020.

[9] M. J. Yu *et al.*, "Fractional-order modeling of lithium-ion batteries using additive noise assisted modeling and correlative information criterion," (in English), *Journal of Advanced Research,* vol. 25, pp. 49-56, Sep 2020.

[10] X. S. Hu, D. P. Cao, and B. Egardt, "Condition Monitoring in Advanced Battery Management Systems: Moving Horizon Estimation Using a Reduced Electrochemical Model," (in English), *Ieee-Asme Transactions on Mechatronics,* vol. 23, no. 1, pp. 167-178, Feb 2018.

[11] Y. Xie, X. S. Hu, C. F. Zou, F. Feng, and X. L. Tang, "Novel Mesoscale Electrothermal Modeling for Lithium-Ion Batteries," (in English), *Ieee Transactions on Power Electronics,* vol. 35, no. 3, pp. 2595-2614, Mar 2020.

[12] Y. Xie *et al.*, "A novel electro-thermal coupled model of lithium-ion pouch battery covering heat generation distribution and tab thermal behaviours," (in English), *International Journal Of Energy Research,* vol. 44, no. 14, pp. 11725-11741, Nov 2020.

[13] H. H. Li, X. Y. Wang, A. Saini, Y. Q. Zhu, and Y. P. Wang, "State of Charge Estimation for Lithium-Ion Battery Models Based on a Thermoelectric Coupling Model," (in English), *International Journal Of Electrochemical Science,* vol. 15, no. 5, pp. 3807-3824, May 2020.

[14] T. F. Landinger, G. Schwarzberger, and A. Jossen, "A Physical-Based High-Frequency Model of Cylindrical Lithium-Ion Batteries for Time Domain Simulation," (in English), *Ieee Transactions on Electromagnetic Compatibility,* vol. 62, no. 4, pp. 1524-1533, Aug 2020.

[15] D. Galatro, C. D. Silva, D. A. Romero, O. Trescases, and C. H. Amon, "Challenges in data-based degradation models for lithium-ion batteries," (in English), *International Journal Of Energy Research,* vol. 44, no. 5, pp. 3954-3975, Apr 2020.

[16] R. Drummond, A. M. Bizeray, D. A. Howey, and S. R. Duncan, "A Feedback Interpretation of the Doyle-Fuller-Newman Lithium-Ion Battery Model," (in English), *Ieee Transactions on Control Systems Technology,* vol. 28, no. 4, pp. 1284-1295, Jul 2020.

[17] Y. Q. Shen, "Adaptive extended Kalman filter based state of charge determination for lithium-ion batteries," (in English), *Electrochimica Acta,* vol. 283, pp. 1432-1440, Sep 1 2018.

[18] X. P. Chen *et al.*, "Dynamic behavior and modeling of prismatic lithium-ion battery," (in English), *International Journal Of Energy Research,* vol. 44, no. 4, pp. 2984-2997, Mar 25 2020.

[19] L. G. Chen *et al.*, "Core temperature estimation based on electro-thermal model of lithium-ion batteries," (in English), *International Journal of Energy Research,* vol. 44, no. 7, pp. 5320-5333, Jun 10 2020.

[20] S. Barcellona and L. Piegari, "Integrated electro-thermal model for pouch lithium ion batteries," (in English), *Mathematics And Computers In Simulation,* vol. 183, pp. 5-19, May 2021.

[21] K. Stinson, "On Gamma-Convergence of a Variational Model for Lithium-Ion Batteries," (in English), *Archive for Rational Mechanics And Analysis,* vol. 240, no. 1, pp. 1-50, Apr 2021.

[22] S. L. Wang *et al.*, "A novel safety assurance method based on the compound equivalent modeling and iterate reduce particle-adaptive Kalman filtering for the unmanned aerial vehicle lithium ion batteries," (in English), *Energy Science & Engineering,* vol. 8, no. 5, pp. 1484-1500, May 2020.

[23] S. B. Vilsen, S. K. Kaer, and D. I. Stroe, "Log-Linear Model for Predicting the Lithium-ion Battery Age Based on Resistance Extraction from Dynamic Aging Profiles," (in English), *Ieee Transactions on Industry Applications,* vol. 56, no. 6, pp. 6937-6948, Nov 2020.

[24] S. Tang *et al.*, "Electrochemical behavior simulation of high specific energy power lithium-ion batteries based on numerical model," (in English), *Ionics,* vol. 26, no. 11, pp. 5513-5523, Nov 2020.

[25] Y. Q. Tan, M. J. Luo, L. Y. She, and X. Y. Cui, "Joint Estimation of Ternary Lithium-ion Battery State of Charge and State of Power Based on Dual Polarization Model," (in English), *International Journal Of Electrochemical Science,* vol. 15, no. 2, pp. 1128-1147, Feb 2020.

[26] Z. Ren, C. Q. Du, H. W. Wang, and J. B. Shao, "Error Analysis of Model-based State-of-Charge Estimation for Lithium-Ion Batteries at Different Temperatures," (in English), *International Journal Of Electrochemical Science,* vol. 15, no. 10, pp. 9981-10006, Oct 2020.

[27] U. Morali and S. Erol, "Analysis of electrochemical impedance spectroscopy response for commercial lithium-ion batteries: modeling of equivalent circuit elements," (in English), *Turkish Journal of Chemistry,* vol. 44, no. 3, pp. 602-613, 2020.

[28] H. Miao, J. J. Chen, L. Mao, K. Q. Qu, J. B. Zhao, and Y. J. Zhu, "A novel online model parameters identification method with anti-interference characteristics for lithium-ion batteries," (in English), *International Journal Of Energy Research,* vol. 45, no. 6, pp. 9502-9517, May 2021.

[29] J. F. Jia, K. K. Wang, X. Q. Pang, Y. H. Shi, J. Wen, and J. C. Zeng, "Multi-Scale Prediction of RUL and SOH for Lithium-Ion Batteries Based on WNN-UPF Combined Model," (in English), *Chinese Journal Of Electronics,* vol. 30, no. 1, pp. 26-35, Jan 2021.

[30] W. X. Duan, C. X. Song, S. L. Peng, F. Xiao, Y. L. Shao, and S. X. Song, "An Improved Gated Recurrent Unit Network Model for State-of-Charge Estimation of Lithium-Ion Battery," (in English), *Energies,* vol. 13, no. 23, pp. 1-11, Dec 2020.

[31] M. Li, Y. J. Zhang, Z. L. Hu, Y. Zhang, and J. Zhang, "A Battery SOC Estimation Method Based on AFFRLS-EKF," (in English), *Sensors,* vol. 21, no. 17, pp. 1-13, Sep 2021.

[32] X. W. Guo, X. Z. Xu, J. H. Geng, X. Hua, Y. Gao, and Z. Liu, "SOC Estimation with an Adaptive Unscented Kalman Filter Based on Model Parameter Optimization," (in English), *Applied Sciences-Basel,* vol. 9, no. 19, pp. 1-10, Oct 2019.

[33] M. Gholizadeh and A. Yazdizadeh, "Systematic mixed adaptive observer and EKF approach to estimate SOC and SOH of lithium-ion battery," (in English), *Iet Electrical Systems in Transportation,* vol. 10, no. 2, pp. 135-143, Jun 2020.

[34] L. Feng, J. Ding, and Y. Y. Han, "Improved sliding mode based EKF for the SOC estimation of lithium-ion batteries," (in English), *Ionics,* vol. 26, no. 6, pp. 2875-2882, Jun 2020.

[35] Z. H. Cen and P. Kubiak, "Lithium-ion battery SOC/SOH adaptive estimation via simplified single particle model," (in English), *International Journal Of Energy Research,* vol. 44, no. 15, pp. 12444-12459, Dec 2020.

[36] X. Huang, X. N. Feng, X. B. Han, L. G. Lu, and M. G. Ouyang, "Study on Modeling, Experimentation and State of Charge Estimation of Parallel Connected Lithium-ion Batteries," (in English), *International Journal Of Electrochemical Science,* vol. 15, no. 2, pp. 1264-1286, Feb 2020.

[37] M. G. Hennessy and I. R. Moyles, "Asymptotic reduction and homogenization of a thermo-electrochemical model for a lithium-ion battery," (in English), *Applied Mathematical Modelling,* vol. 80, pp. 724-754, Apr 2020.

[38] S. Hein, T. Danner, and A. Latz, "An Electrochemical Model of Lithium Plating and Stripping in Lithium Ion Batteries," (in English), *Acs Applied Energy Materials,* vol. 3, no. 9, pp. 8519-8531, Sep 28 2020.

[39] T. Tan, K. N. Chen, Q. Q. Lin, Y. Jiang, L. Q. Yuan, and Z. M. Zhao, "An Approach to Estimate Lithium-Ion Battery State of Charge Based on Adaptive Lyapunov Super Twisting Observer," (in English), *Ieee Transactions on Circuits And Systems I-Regular Papers,* vol. 68, no. 3, pp. 1354-1365, Mar 2021.

[40] P. Shrivastava, T. K. Soon, M. Y. I. Bin Idris, S. Mekhilef, and S. B. R. S. Adnan, "Combined State of Charge and State of Energy Estimation of Lithium-Ion Battery Using Dual Forgetting Factor-Based Adaptive Extended Kalman Filter for Electric Vehicle Applications," (in English), *Ieee Transactions on Vehicular Technology,* vol. 70, no. 2, pp. 1200-1215, Feb 2021.

[41] Z. C. He, Z. M. Yang, X. Y. Cui, and E. Li, "A Method of State-of-Charge Estimation for EV Power Lithium-Ion Battery Using a Novel Adaptive Extended Kalman Filter," (in English), *Ieee Transactions on Vehicular Technology,* vol. 69, no. 12, pp. 14618-14630, Dec 2020.

[42] X. S. Hu, H. Yuan, C. F. Zou, Z. Li, and L. Zhang, "Co-Estimation of State of Charge and State of Health for Lithium-Ion Batteries Based on Fractional-Order Calculus," (in English), *IEEE Transactions on Vehicular Technology,* vol. 67, no. 11, pp. 10319-10329, Nov 2018.

[43] G. Sethia, S. Majhi, S. K. Nayak, and S. Mitra, "Strict Lyapunov super twisting observer design for state of charge prediction of lithium-ion batteries," (in English), *IET Renewable Power Generation,* vol. 15, no. 2, pp. 424-435, Feb 2021.

[44] B. Rente *et al.*, "Lithium-Ion Battery State-of-Charge Estimator Based on FBG-Based Strain Sensor and Employing Machine Learning," (in English), *Ieee Sensors Journal,* vol. 21, no. 2, pp. 1453-1460, Jan 15 2021.

[45] B. Haus and P. Mercorelli, "Polynomial Augmented Extended Kalman Filter to Estimate the State of Charge of Lithium-Ion Batteries," (in English), *Ieee Transactions on Vehicular Technology,* vol. 69, no. 2, pp. 1452-1463, Feb 2020.

[46] Y. Feng, C. Xue, Q. L. Han, F. L. Han, and J. C. Du, "Robust Estimation for State-of-Charge and State-of-Health of Lithium-Ion Batteries Using Integral-Type Terminal Sliding-Mode Observers," (in English), *Ieee Transactions on Industrial Electronics,* vol. 67, no. 5, pp. 4013-4023, May 2020.

[47] B. Xiao, B. Xiao, and L. S. Liu, "Rapid measurement method for lithium-ion battery state of health estimation based on least squares support vector regression," (in English), *International Journal of Energy Research,* vol. 45, no. 4, pp. 5695-5709, Mar 25 2021.

[48] H. X. Tian and P. L. Qin, "State of health prediction for lithium-ion batteries with a novel online sequential extreme learning machine method," (in English), *International Journal Of Energy Research,* vol. 45, no. 2, pp. 2383-2397, Feb 2021.

[49] C. I. Ossai and I. P. Egwutuoha, "Real-time state-of-health monitoring of lithium-ion battery with anomaly detection, Levenberg-Marquardt algorithm, and multiphase exponential regression model," (in English), *Neural Computing & Applications,* vol. 33, no. 4, pp. 1193-1206, Feb 2021.

[50] J. S. Yu, J. Yang, Y. Wu, D. Y. Tang, and J. Dai, "Online state-of-health prediction of lithium-ion batteries with limited labeled data," (in English), *International Journal Of Energy Research,* vol. 44, no. 14, pp. 11345-11353, Nov 2020.

[51] L. Ungurean, M. V. Micea, and G. Carstoiu, "Online state of health prediction method for lithium-ion batteries, based on gated recurrent unit neural networks," (in English), *International Journal Of Energy Research,* vol. 44, no. 8, pp. 6767-6777, Jun 25 2020.

[52] J. P. Tian, R. Xiong, and W. X. Shen, "State-of-Health Estimation Based on Differential Temperature for Lithium Ion Batteries," (in English), *Ieee Transactions on Power Electronics,* vol. 35, no. 10, pp. 10363-10373, Oct. 2020.

[53] Y. D. Tan and G. C. Zhao, "Transfer Learning With Long Short-Term Memory Network for State-of-Health Prediction of Lithium-Ion Batteries," (in English), *Ieee Transactions on Industrial Electronics,* vol. 67, no. 10, pp. 8723-8731, Oct. 2020.

[54] D. I. Stroe and E. Schaltz, "Lithium-Ion Battery State-of-Health Estimation Using the Incremental Capacity Analysis Technique," (in English), *IEEE Transactions on Industry Applications,* vol. 56, no. 1, pp. 678-685, Jan-Feb 2020.

[55] Z. Y. Song *et al.*, "The sequential algorithm for combined state of charge and state of health estimation of lithium-ion battery based on active current injection," (in English), *Energy,* vol. 193, pp. 66-77, Feb 15 2020.

[56] Y. Z. Gao *et al.*, "Health-Aware Multiobjective Optimal Charging Strategy With Coupled Electrochemical-Thermal-Aging Model for Lithium-Ion Battery," (in English), *IEEE Transactions on Industrial Informatics,* vol. 16, no. 5, pp. 3417-3429, May 2020.

[57] J. Cao, D. Harrold, Z. Fan, T. Morstyn, D. Healey, and K. Li, "Deep Reinforcement Learning-Based Energy Storage Arbitrage With Accurate Lithium-Ion Battery Degradation Model," (in English), *Ieee Transactions on Smart Grid,* vol. 11, no. 5, pp. 4513-4521, Sept 2020.

[58] M. Safdari, S. Sadeghzadeh, and R. Ahmadi, "Tailoring the life cycle of lithium-ion batteries with a passive cooling system: A comprehensive dynamic model," (in English), *International Journal Of Energy Research,* vol. 45, no. 5, pp. 7884-7902, Apr 2021.

[59] H. J. Ruan, B. X. Sun, W. G. Zhang, X. J. Su, and X. T. He, "Quantitative Analysis of Performance Decrease and Fast-Charging Limitation for Lithium-Ion Batteries at Low Temperature Based on the Electrochemical Model," (in English), *Ieee Transactions on Intelligent Transportation Systems,* vol. 22, no. 1, pp. 640-650, Jan 2021.

[60] T. Mesbahi, P. Bartholomeus, N. Rizoug, R. Sadoun, F. Khenfri, and P. Le Moigne, "Advanced Model of Hybrid Energy Storage System Integrating Lithium-Ion Battery and Supercapacitor for Electric Vehicle Applications," (in English), *Ieee Transactions on Industrial Electronics,* vol. 68, no. 5, pp. 3962-3972, May 2021.

[61] J. Y. Lu *et al.*, "Mathematical Modeling and Frequency-Domain Characteristics of a Periodic Pulse-Discharged Lithium-Ion Battery System," (in English), *Ieee Transactions on Industry Applications,* vol. 57, no. 2, pp. 1801-1809, Mar-Apr 2021.

CRediT author statement

Shunli Wang: Conceptualization, Methodology, Software.

Paul Takyi-Aninakwa: Writing, and Presentation optimization.

Yongcun Fan: Methodology.

Chunmei Yu: Visualization, Investigation.

Siyu Jin: Software, Validation.

Carlos Fernandez: Data curation, Writing, and Original draft preparation.

Daniel-Ioan Stroe: Writing- Reviewing and Editing.